Selenium Migration and SiC Structural Evolution Post Helium and Selenium Co-implantation and Annealing

S. Mthalane[1], H.A.A. Abdelbagi[1], C.B. Mtshali[2], B.S. Li[3], V.A. Skuratov [4,5,6], S.S Ntshangase[1] T.T. Hlatshwayo[7]*

[1]*Physics Department, University of Zululand, KwaDlangezwa, 3886, South Africa*
[2]*Materials Research Department, iThemba LABS, P.O. Box 722, Somerset West, 7129, South Africa*
[3]*State Key Laboratory for Environment-friendly Energy Materials, Southwest, University of Science and Technology, Mianyang, Sichuan 621010, China*
[4]*Joint Institute for Nuclear Research, Dubna, Russia*
[5]*Dubna State University, Dubna, Moscow Region, Russia*
[6]*National Research Nuclear University MEPhI, Moscow, Russia*
[7]*Physics Department, University of Pretoria, Pretoria, 0002, South Africa*

Abstract

Polycrystalline SiC samples were first implanted with 200 keV selenium (Se) ions at room temperature (RT) to a fluence of 1×10^{16} cm^{-2}. Thereafter, some of the pre-implanted SiC samples were separately implanted with helium (He) ions of 17 keV to a fluence of 1×10^{17} cm^{-2} at RT and 500 °C. The samples were then annealed in a vacuum at 1000 °C for 5 h. Raman spectroscopy and transmission electron microscopy (TEM) were used to study the influence of Se and He co-implantation and annealing on the microstructure of SiC. Rutherford backscattering spectrometry (RBS) was used to study the migration behavior of Se in SiC before and after co-implantation and annealing. Implantation of Se at RT amorphized the SiC near the surface implanted region. Co-implantation at RT created a high portion of free carbon atoms in the damaged region accompanied by the formation of He nano-bubbles, while co-implantation at 500 °C led to some recrystallization of initially amorphous SiC and formation of larger He bubbles. Annealing at 1000 °C caused some recrystallization in both as-implanted (SiC implanted with Se only) and co-implanted samples. However, the recrystallization was accompanied by the formation of graphite crystals (with an average size of 10 nm) in the samples co-implanted at RT. This indicates that co-implantation at RT induces more detrimental effects on the physical integrity of SiC. RBS results showed no change in Se distribution in SiC after subsequent implantation with He ions at RT and 500 °C. However, annealing at 1000 °C caused the Se atoms to migrate towards the bulk of SiC in the co-implanted samples, while no significant migration of Se atoms was observed in the as-implanted

samples (SiC implanted with Se only) annealed under the same conditions. This suggests that He assisted Se migration in SiC.

Keywords: SiC, Co-implantation, Selenium, He-bubbles, recrystallization.

*Corresponding author: Heshamabdelbagi100@gmail.com

1. Introduction

Currently, over 83% of global electricity is generated by burning fossil fuels, primarily coal, natural gas, and petroleum. These sources have been the primary energy source for decades due to their abundance and ease of extraction [1]. However, burning fossil fuels has negative consequences for the environment and human health and welfare. Consequently, the development of carbon-free, environmentally friendly, and sustainable forms of energy has emerged as a crucial global priority. Hydro, wind, solar, and nuclear energy have emerged as promising candidates for this transition [1, 2]. However, nuclear energy receives a lower degree of favorability due to safety concerns associated with the release of radioactive fission products (FPs) into the environment and the challenges faced in managing nuclear waste storage.

The new design of nuclear fuels for high-temperature gas-cooled reactors (HTGCRs), including pebble bed modular reactors (PBMR), encapsulates the fuel kernel in four layers using chemical vapour deposition (CVD), which allows the fuel structure to contain most of the FPs throughout normal reactor operation [3, 4]. This type of fuel is known as a tri-structural isotropic (TRISO) particle which consists of an inner core of uranium dioxide (UO_2) surrounded by four CVD layers namely: a porous carbon buffer layer, an inner pyrolytic carbon (IPyC) layer, a silicon carbide (SiC) layer, and an outer pyrolytic carbon (OPyC) layer [4]. The purpose of the first layer (i.e., a porous carbon buffer layer) is to accommodate internal gas accumulation, while the IPyC layer serves as a diffusion barrier for most non-metallic FPs, SiC serves as the primary diffusion barrier for metallic FPs, and OPyC helps in reducing stress within SiC by shielding it from external chemical and mechanical interactions [5, 6].

Due to its outstanding properties, including its extreme hardness, temperature stability, radiation resistance, thermal conductivity, and small neutron absorption cross-sections, SiC was selected to serve as the main diffusion barrier for FPs in TRISO particles. Depending on the

stacking order, SiC can exist in more than 200 polytypes in different forms (such as 3C, 4H, 6H, and 15R) [7]. However, for nuclear reactor applications, particularly in TRISO fuel particles, a polycrystalline material with a 3C–SiC structure is ideal. A key reason for this preference is the high radiation resistance of 3C-SiC to neutron bombardment compared to single-crystal SiC [8].

TRISO particles retain the majority of FPs during nuclear reactor operation, except silver (Ag), xenon (Xe), krypton (Kr), europium (Eu), and strontium (Sr) [9]. Since SiC is the major diffusion barrier in TRISO particles, ion implantation and annealing processes have been used to understand the migration behavior of these FPs in SiC over the past four decades [10-15]. Based on these studies, it was found that radiation damage caused by ion implantation in SiC structures significantly affected the migration of FPs. Moreover, the migration and interaction of other FPs (that had not been detected outside of the TRISO particle, such as palladium (Pd)) with SiC were investigated to study their effect on the integrity of SiC as well as their impact on the migration of some FPs [16-18]. In addition to that, the effect of swift heavy ions (SHIs) irradiation on the migration behavior of FPs (such as Ag [19], Sr [20], and Se [21]) was also investigated. These studies were done to understand the effects of some factors (i.e., those present in a nuclear reactor environment, such as ion bombardment, high temperatures, and SHIs) on the migration of FPs in SiC. According to these studies, implantation at room temperature (RT) amorphizes SiC, while SHIs cause some recrystallization and enhance FPs migration after annealing, and Pd interacts with SiC which reduces its integrity.

During the fission process in the fuel kernel, not only FPs are produced, but also helium (He) can be generated as a result of the alpha-decay of actinide elements (by neutron capture) as well as neutronic transmutation [22]. Recently, the effect of He on SiC integrity as well as on the migration of some FPs, such as Ag [23, 24] and Sr [25, 26] and non-FPs such as magnesium (Mg) [27] and iron (Fe) [28] was investigated. It has been reported that He forms bubbles within SiC [29]. These bubbles may adversely affect SiC integrity [30]. Therefore, SiC would lose its legitimacy as a primary diffusion barrier of FPs if this integrity were compromised. However, the formation of cavities caused by He bubbles in SiC traps Ag, Sr and Fe atoms [24, 26, 28]. Meanwhile, He bubbles (not cavities formed after the bubbles leave) enhanced the migration of Ag and Sr by creating pores on the surface of SiC that allowed these FPs to diffuse out [23, 25]. Consequently, the presence of He bubbles in SiC has both advantages and disadvantages. At 1000

°C (similar to the nuclear operating temperature), He diffuses out of SiC material leaving cavities that trap Ag and Sr FPs from diffusion. On the other hand, it could reduce the integrity of SiC. As a result, further investigation is needed to gain a better understanding of the role of He in SiC integrity and the migration of other FPs (other than Ag and Sr).

Selenium (Se) is a non-metallic element with many radioactive and stable isotopes. ^{79}Se is a radioactive isotope that is found in the FPs of uranium [31]. During its radioactive decay, selenium emits beta particles, which are associated with increased cancer risk [32]. So far, only a few studies have been done on Se migration in SiC [21, 33-35]. In these studies, the Se implanted SiC samples were vacuum annealed at temperatures ranging from 1000 to 1500 °C [33-35], and another set of samples were irradiated by SHIs [21]. They found that Se migration in SiC began at temperatures higher than 1200 °C, while no migration of Se was observed upon irradiation by SHIs. As a result, this indicates that Se has a low diffusivity in SiC at temperatures < 1300 °C. To the best of our knowledge, the role of He on Se migration in SiC has not been investigated. The effect of He on Se migration needs to be investigated to get a better understanding of the migration of this fission product in SiC.

In this study, we investigated the changes in the microstructure of polycrystalline SiC caused by co-implantation of Se at RT and He at RT and 500°C, followed by annealing at 1000°C. Additionally, Se migration in the as-implanted SiC (implanted with Se only) and co-implanted SiC samples was investigated after annealing at 1000°C and compared with previous studies [26, 33-35].

2. Experimental procedure

Polycrystalline SiC wafers were obtained from Valley Design Corporation for use in this study. These starting materials were consisting mainly of columnar crystallites aligned along the growth direction, with diameters of a few micrometers, as reported in [36]. Furthermore, the lattice structure of the SiC crystals was predominantly cubic, although some hexagonal growth modes were also observed [36]. SiC wafers were implanted under vacuum with Se ions of 200 keV to a fluence of 1×10^{16} cm^{-2} at RT. The implantation was performed at the Friedrich-Schiller-University Jena, in Germany. After implanting Se ions, the samples were separately implanted with He ions

of 17 keV to a fluence of 1×10^{17} cm^{-2} at RT and 500 °C, respectively. The implantation of He was performed at iThemba LABS in South Africa.

To simulate the distribution of Se and He ions implanted in SiC, SRIM (Stopping and Range of Ions in Matter 2013 [37]) software was used before the implantation process was carried out. Simulations were performed to select the energies of the ions that would allow Se and He depth profiles to overlap in SiC. In the simulation, threshold displacement energies of 35 and 20 eV were used for Si and C atoms, respectively. As sintered SiC has a low density of 3.21 g/cm^3 [38], this value was also used in the simulation.

Fig. 1 shows the simulated concentration distributions of Se and He in the co-implanted samples together with the simulated lattice damage (in displacement per atom (dpa)) caused by individual implantation of Se and He ions and the total dpa caused by co-implantation. The arrows in Fig. 1 indicate the maximum relative atomic density and maximum lattice damage, as well as their depth within the sample. The implanted Se exhibited a maximum relative atomic density of 1.5% at a depth of 90 nm and a maximum lattice damage (in dpa) of 1.3 dpa at 70 nm below the surface. In addition, implanted He reached a maximum relative atomic density of 11.8% at a depth of 130 nm and a maximum dpa of 3.8 dpa at 100 nm below the surface. The high relative atomic density of He in SiC, along with the elevated dpa, can be attributed to the high fluence of He ions. Furthermore, the co-implanted SiC samples exhibited a total maximum dpa of 4.8 at a depth of 90 nm below the surface. This value is higher than that observed in the individually implanted samples, likely due to the interaction of defects [26]. Based on these simulation results, it appears that the Se and He depth profiles overlap, allowing a study of their synergistic effects on the structural evolution of SiC and the role that He bubbles play in Se migration. Furthermore, if 0.3 dpa is required to amorphize SiC [39], about 125 nm of the SiC layer will be amorphized by Se ions only, which is consistent with previous studies [33-34]. However, He ions resulted in a greater amorphous region thickness of about 175 nm.

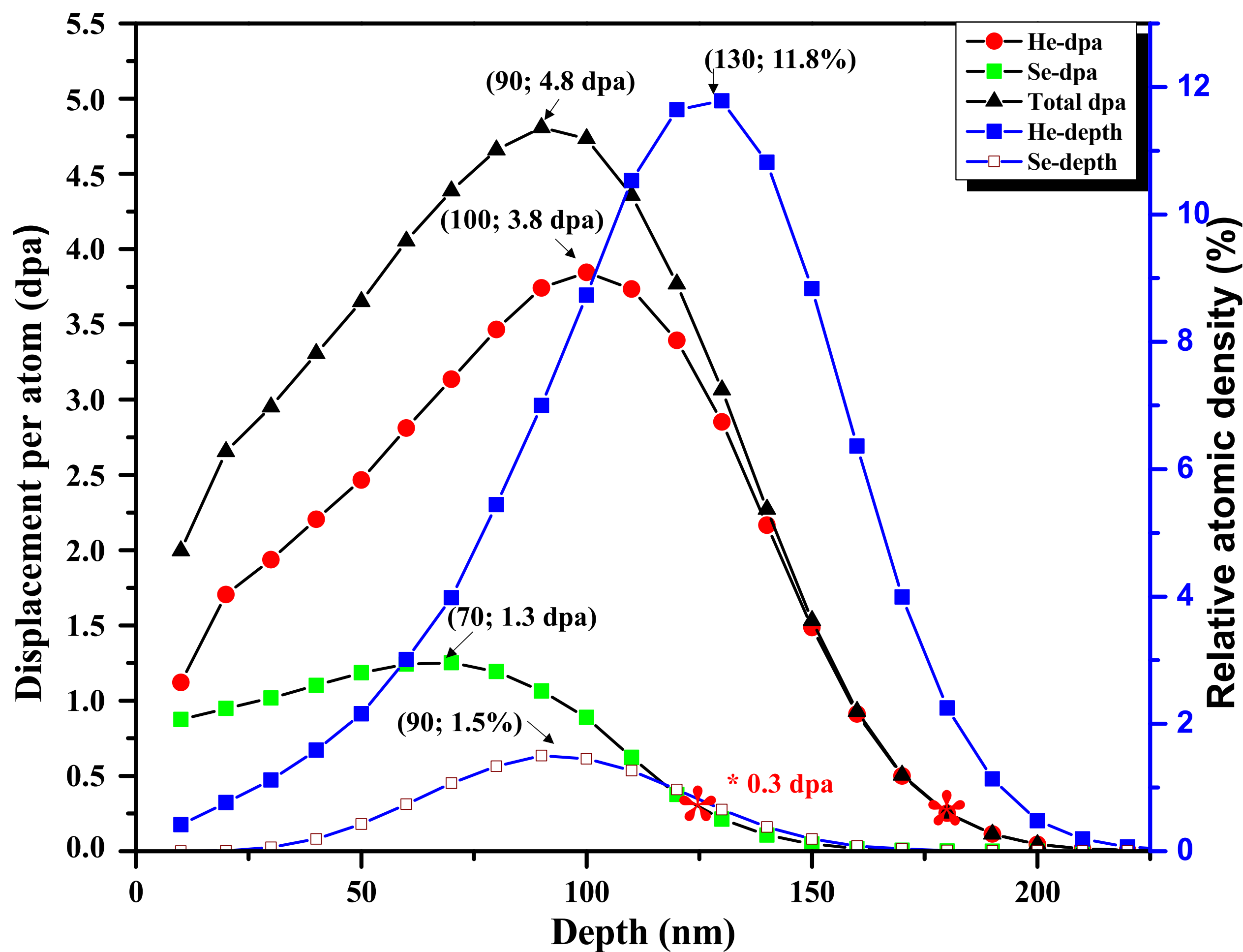

Fig. 1: *The relative atomic density and displacement per atom (dpa) in SiC implanted with Se and He ions were calculated using SRIM simulations. Red stars indicate the depths corresponding to 0.3 dpa for both Se and He, along with their total contributions.*

As-implanted (SiC implanted with Se only) and co-implanted SiC samples were annealed under vacuum (10^{-5} Pa) at 1000 °C for 5 h using a quartz tube furnace. Annealing was conducted at 1000 °C to simulate reactor operation conditions of modern nuclear reactors, where the normal reactor temperature is approximately 1000 °C. Raman spectroscopy and transmission electron microscopy (TEM) were used to investigate microstructural changes in virgin SiC after implantation with Se and He, and annealing. Moreover, Rutherford backscattering spectrometry (RBS) was used to study Se migration in both as-implanted and co-implanted samples after annealing.

The RBS analysis was performed at iThemba LABS using 2 MeV helium ions (He^+). The beam spot size was about 1 mm. A silicon (Si) surface barrier detector was used to detect backscattered He ions at 150° scattering angle. In each measurement, a constant current of approximately 500 pA was maintained, and a total charge of 500 nC was collected. Se profiles in energy channels were converted into depth profiles using Ziegler, Biersack, and Littmark (ZBL) stopping powers [37] and a SiC density of 3.21 gcm^{-3}.

WITec alpha 300 confocal Raman spectroscopy instrument was used to monitor the influence of individual implantation of Se, co-implantation of Se and He, and annealing on the microstructure of SiC substrate. Using a 100×0.9NA objective lens, Raman spectra were acquired at 532nm with 5mW laser excitation. SiC Raman spectra were analyzed by first correcting the baseline of the spectral lines using a linear background correction. Subsequently, using the OriginLab software program [40], the spectra were fitted using the Gaussian function to determine the full width at half maximum (FWHM) and peak positions.

Two different FIB instruments were used in this study to prepare the lamellae. In the first FIB instrument, two platinum layers were sequentially deposited using electron and Ga ion beam respectively in order to protect the lamellae surface during the slicing process. Owing to some problems with the platinum source in the second FIB instrument carbon layers were used as protecting layers in the other lamellae. During the lamella thinning process, Ga ions with an initial energy of 30 keV were used. The ion energy was then gradually reduced in several steps down to 2 keV to minimize damage and obtain lamellae with final thicknesses below 100 nm. After lamella preparation, TEM analysis was performed using the JEOL JEM 2100F field emission transmission electron microscope operating at 200 kV. Some samples were analyzed using the Thermoscientific Talos F200i TEM at 200 kV as well. Moreover, energy-dispersive X-ray spectroscopy (EDS) was used to study the composition of the samples before and after annealing. The details of each TEM image (i.e., which TEM system it was taken with) are provided in the results section.

3. Results and discussion

3.1 Raman results:

Fig. 2 shows Raman spectra of virgin SiC after implantation (with Se at RT), co-implantation (with Se and He at RT and 500 °C), and annealing. The spectra of the virgin samples show sharp and well resolved peaks centered around 766, 792 and 964 cm^{-1}. The peaks located around 792 and 964 cm^{-1} are attributed to the 3C-SiC transverse optical (TO) and longitudinal optical (LO) signatures, respectively. The peak located around 766 cm^{-1} represents the TO phonon mode of hexagonal polytype 6H-SiC [41], which indicates the presence of a small fraction of hexagonal polytypes within the 3C-SiC layer. Moreover, the low intense peaks at ~1515 cm^{-1} and ~1710 cm^{-1}, respectively, represent the second order peaks of TO [42, 43], which indicate the good crystalline quality of the virgin SiC wafers. However, all virgin SiC Raman peaks disappeared after implantation with Se at RT and broad peaks appeared instead – see Fig. 2 (a). The three broad Raman bands observed after Se implantation are centered around 425, 750 and 1300 cm^{-1} and correspond to the vibrations of Si-Si, Si-C, and C-C bonds, respectively. Observing these changes indicates that the SiC layer becomes amorphized after implantation with Se ions at RT. This was predicted by SRIM as shown in Fig. 1.

Raman spectra of SiC samples implanted with Se ions at RT then subsequently implanted with He ions at RT and 500 °C are shown in Fig. 2 (a). He implanted at RT resulted in an increase in the intensity of C-C peak compared to Si-Si and Si-C peaks, indicating that carbon clusters are formed within the amorphous layer. Li *et al.* [44] observed similar results after irradiating polycrystalline α-SiC with 300 keV He ions at a fluence of 7.3×10^{17} cm^{-2} at room temperature. They found that carbon clusters are due to the lower migration energy of carbon atoms (compared to Si atoms) which migrate more easily and accumulate in vacancy regions after He implantation [45], increasing C levels at certain positions as a result. On the other hand, the Se implanted samples that were subsequently implanted with He at 500 °C showed the reappearance of SiC characteristic Raman peaks at around 766, 795 and 964 cm^{-1}, indicating the recrystallization of the initially amorphized layer. One would expect to see more defects in the 500 °C co-implanted samples (more than in the Se implanted samples) due to the high fluence of He ions (i.e., $1\times10^{17}cm^{-2}$), but the recrystallization here is due to the implantation temperature which causes defect

recovery. However, some defects in the 500 °C co-implanted SiC structure are still present (i.e., Si-Si peak at around 525 cm^{-1}).

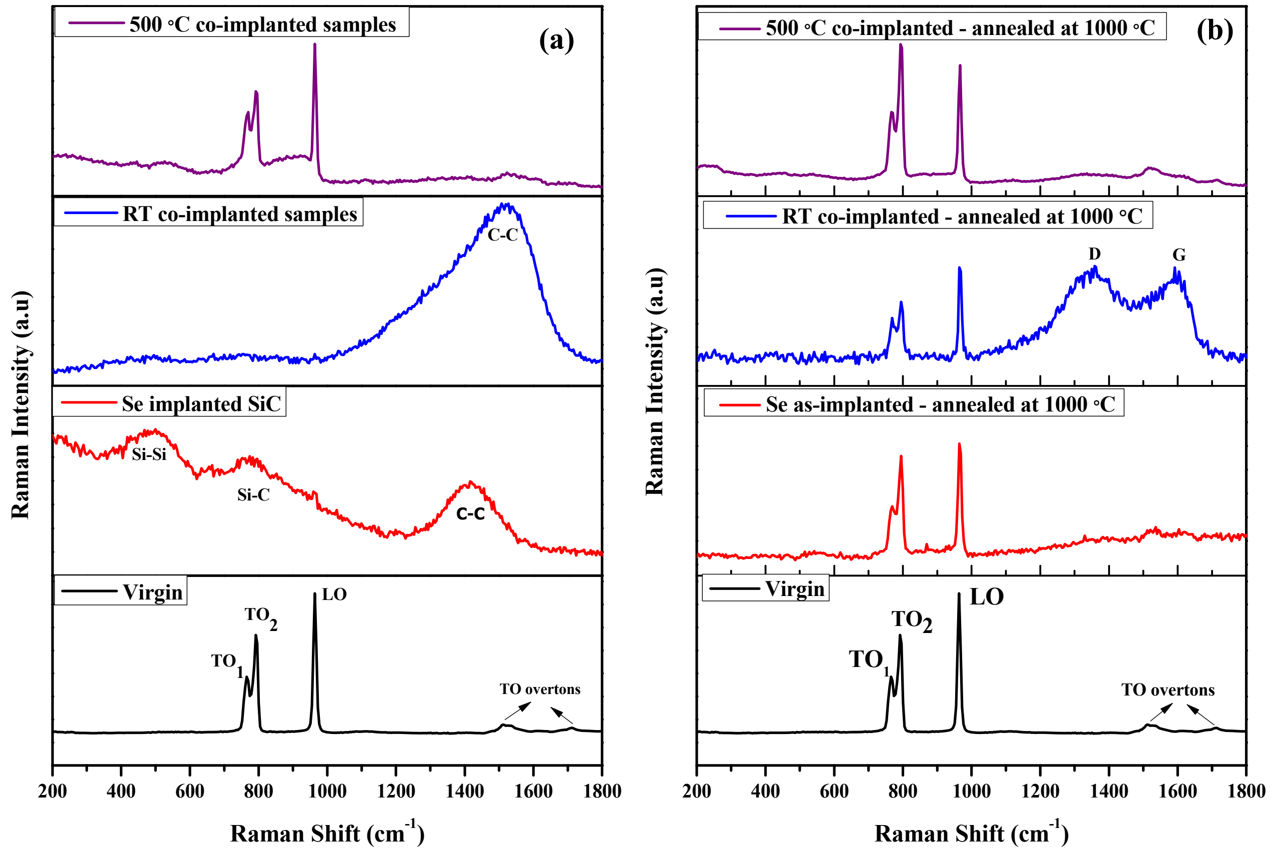

***Fig. 2:** Raman spectra of virgin SiC after (a) implantation with Se ions at RT and (b) co-implantation with Se at RT and He at 500 °C, all annealed at 1000 °C.*

Fig. 2 (b) shows the Raman spectra of as-implanted (SiC implanted with Se only) and co-implanted (Se+He at RT and 500 °C) samples annealed at 1000 °C. Annealing the Se implanted samples resulted in recrystallization (i.e., reappearance of SiC characteristic Raman peaks) of initially amorphous SiC with a significant shift of the TO peaks toward higher wavenumbers (compared to the virgin SiC). This indicates that annealing caused compressive stress in Se implanted samples. Fig. 3 below shows stress amounts in virgin, implanted and annealed samples. Moreover, in the RT co-implanted samples, the reappearance of TO and LO peaks after annealing was accompanied by the appearance of the D and G characteristic bands at positions 1346 cm^{-1} and 1587 cm^{-1}, respectively. This indicates that the carbon clusters in the RT co-implanted samples

enhanced the formation of some graphite crystals within the implanted region after annealing at 1000 °C. The graphite average crystal size was calculated from the I_D/I_G intensity ratio and found to be 10 nm. Moreover, annealing the 500 °C co-implanted samples at 1000 °C caused the disappearance of the Si-Si peak (shown before annealing) and an increase in the intensity of the TO peak at 792 cm^{-1}. This indicates the decrease in SiC chemical disorder after annealing (i.e., more recrystallization) [26].

The average stress in the samples was calculated using both TO and LO Raman peak positions (see equation 12 in [46]). Since the Raman spectra of virgin SiC was used as a reference, stress was assumed to be 0. Implantation of Se at RT caused the disappearance of the sharp LO and TO peaks, therefore, the amount of stress cannot be measured from this sample. However, after co-implantation at 500 °C the stress was -0.25 GPa. This indicates that co-implantation creates compressive stress in SiC. This is due to radiation-induced swelling, which increases compressive stress in SiC [47]. Our results are consistent with previous study [25], where compressive stress was observed in SiC after co-implantation with both Sr and He at temperatures above critical amorphization temperatures (for SiC, this is around 350 °C [48]). Moreover, annealing increased compressive stress – see Fig. 3. It is known that annealing causes more compressive stress in implanted SiC [25, 49-50], however, the co-implanted samples showed less compressive stress than in Se implanted samples annealed under the same conditions. Previous studies found that implanted He ions formed large He bubbles after annealing at 1000 °C [24-26] (this was also observed in this study and discussed in section 3.2), as well as caused tensile stresses in regions filled with He bubbles [51]. The tensile stresses in the He bubbles region affected the average stress measured from the co-implanted samples, decreasing the compressive stress value.

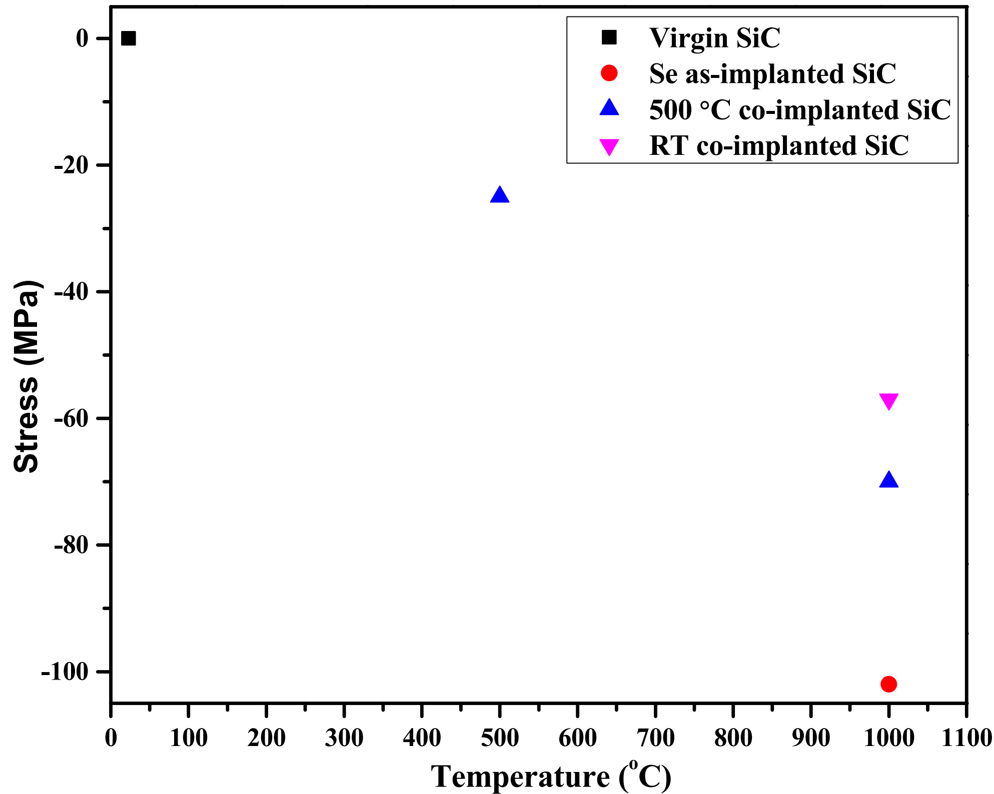

Fig. 3: *The residual stress of virgin, Se implanted and co-implanted samples at RT and 500 °C after annealing at 1000 °C.*

To better understand the amorphization ratio in implanted and annealed samples, chemical disorder was calculated from Raman spectra in Fig. 2. The average chemical disorder in the implanted and annealed samples was calculated from the intensity ratio between the C-C bonds and Si-C bond at around 796 cm-1 [25]. Fig. 4 shows the chemical disorder of Se implanted (implanted with Se only) and co-implanted samples as a function of annealing temperature. Implantation of Se into SiC at RT resulted in chemical disorder equal to 1, suggesting maximum accumulation of chemical disorder and hence, total amorphization [25]. In addition, the chemical disorder for RT co-implanted samples is much greater than 1 due to carbon cluster formation - see Fig. 2. However, co-implantation at 500 °C decreased the chemical disorder value to about 0.8, indicating partial recrystallization of Se implanted SiC samples after subsequent implantation with He ions at 500 ℃. Moreover, annealing reduced chemical disorder in Se implanted and co-implanted samples. Nevertheless, even after annealing, RT co-implanted samples still contain high

disorder due to the formation of graphite crystals within the implanted region – see Fig. 2 and 4. Interestingly, the 500 °C co-implanted samples showed the lowest chemical disorder after annealing at 1000 °C (even less than the Se implanted samples annealed under the same conditions). The difference in the chemical disorder between the samples after annealing might be due to the fact that the initial structure was in a different state before annealing, i.e. the Se implanted samples were amorphous and RT co-implanted samples contained high amounts of free carbon atoms, while 500 °C co-implanted samples were partially recrystallized.

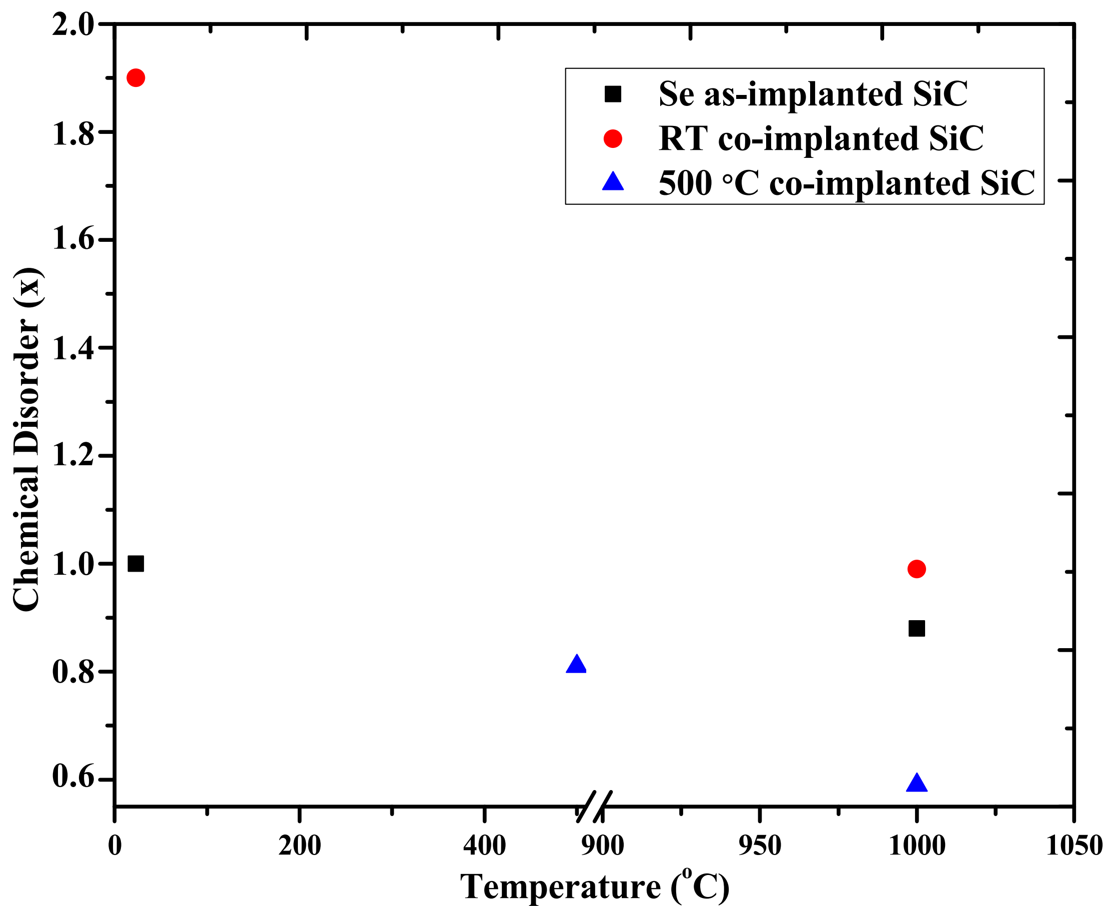

Fig. 4: *Chemical disorder in SiC implanted with Se at room temperature (RT) and co-implanted with Se and He (at RT and 500 °C), before and after annealing at 1000 °C.*

In previous studies [27, 52], He atoms enhanced SiC recrystallization. This could be another explanation for the low chemical disorder in the 500 °C co-implanted samples after annealing. One might wonder why this is not the case with RT co-implanted samples. The answer here is the high

amount of free carbon atoms that inhibited recrystallization and accelerated graphitization after annealing. There were two reasons given in previous studies [27, 52] for He atoms to enhance SiC recrystallization: first, high pressure in bubbles could accelerate crystal nucleation. A second reason is that gas atoms can increase the free energy of the amorphous state, decreasing the minimum size of a thermally stable crystal nucleus.

The third suggestion for differences in chemical disorder after annealing could be attributed to Se migration in SiC. It is known that impurities (except Ag [19, 53] and He [27]) inhibit SiC recrystallization, and Se atoms are considered impurities. Previously, no migration of Se in Se implanted SiC (implanted with Se only) was observed after annealing at 1000 °C [33-35], indicating the presence of Se in the implanted region which reduced recrystallization and increased chemical disorder as a result. In contrast, SiC would readily recrystallize if Se in the 500 °C co-implanted samples migrated from the implanted region. Therefore, the migration behavior of Se in co-implanted samples was investigated using RBS, which will be discussed later in this study (in section 3.3).

3.2 TEM results:

Fig. 5 shows TEM micrographs of the Se implanted SiC before (a) and after co-implantation with He at (b) RT and (c) 500 °C alongside the selected-area electron diffraction (SAED) patterns of their damaged regions. During lamella preparation, platinum (Pt) layers were deposited on the surface of Se implanted samples while for co-implanted samples carbon layers were used as shown in Fig. 5. From Fig. 5 (a), Se ions implantation caused a damaged layer with a thickness of 189 nm below the surface. The SAED patterns in Fig. 5 (b' and c') were obtained from cross-sectional BF TEM micrographs (in focused mode), which are not shown here. A diffuse halo ring is visible in the SAED pattern of Se implanted samples, see Fig. 5 (a'), indicating an amorphous SiC structure. The amorphous layer thickness increased from 189 nm to 230 nm after implanting He ions at RT – see Fig. 5 (b). This was accompanied by the formation of brighter areas (see the blue parallel lines in Fig. 5 (b)) within the implanted region. Since these areas were not observed after implantation with Se only (Fig. 5 (a)), the formation of He nano-bubbles might be responsible for the appearance of these regions after co-implantation with He. In previous studies [26, 44] similar TEM results were reported, and the formation of helium bubbles was explained by the

accumulation of helium atoms in vacancies or interstitial spaces. In the RT co-implanted samples, the SAED pattern confirmed that the structure remained amorphous, see Fig. 5 (b'). However, from Fig. 5 (c'), the SAED pattern in the 500 °C co-implanted indicates that some recrystallization took place within the amorphous region with some defects still present. This was accompanied by a decrease in the amorphous layer thickness and the formation of large He bubbles. The reduction in thickness of the amorphous layer is caused by the epitaxial growth of amorphous SiC at the amorphous-crystalline interface [21]. Moreover, in the RT co-implanted samples, He bubbles with an average size of 3 nm were observed at depths between 75 and 110 nm. Larger He bubbles, with an average size of 6 nm, were present in the range of 110 to 185 nm, followed by the reappearance of smaller bubbles (i.e., with an average size of 3 nm) between 185 and 200 nm. This depth-dependent distribution of bubble sizes is consistent with the He and defect distributions predicted by SRIM, as shown in Fig. 1, where the maximum dpa was observed at 100 nm and the maximum He concentration appeared at 130 nm below the surface. Therefore, vacancies trapped He atoms, leading to the formation of large He bubbles in the region between 110 and 185 nm below the surface. Furthermore, in the 500 °C co-implanted samples, average bubble sizes of 4 nm were observed at depths between 52 and 90 nm. Larger bubbles, with an average size of 11 nm, were observed in the depth range between 90 and 165 nm, while 4 nm bubbles appeared between 165 and 178 nm. He bubbles appeared larger and closer to the surface of SiC (at depths of 52–178 nm) in samples co-implanted at 500 °C, whereas they appeared smaller and deeper (at depths of 75–200 nm) in samples co-implanted at RT. This difference could be attributed to the higher implantation temperature (500 °C), which may have facilitated the migration of He atoms into vacancies, where they were trapped, resulting in the formation of larger He bubbles at shallower depths. Additionally, the thickness of the bubble layer (i.e., the region where He is located in SiC) was not affected by the implantation temperature, remaining around 125 nm in both the RT and 500 °C co-implanted samples.

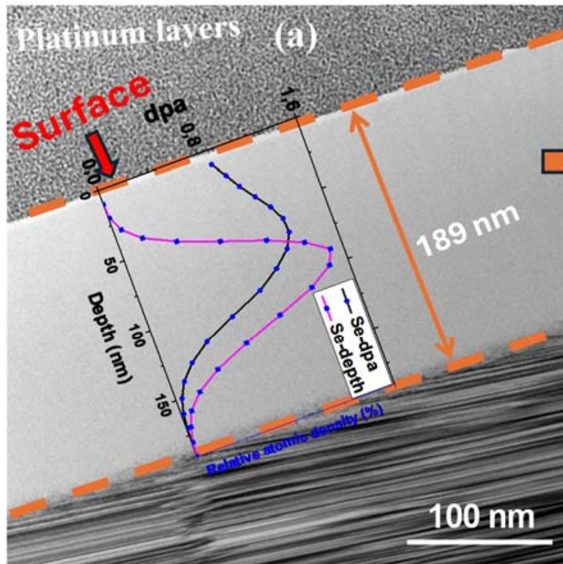
Platinum layers
(a)
Surface
dpa
0.0
0.8
1.6
0
50
100
150
Depth (nm)
Se-dpa
Se-depth
Relative atomic density (%)
189 nm
100 nm

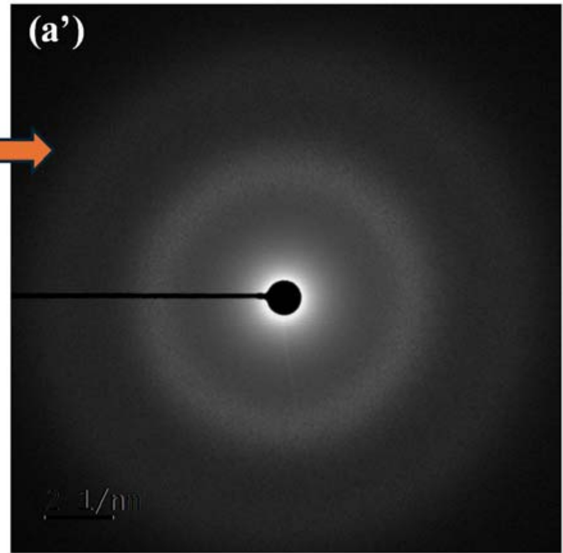
(a')

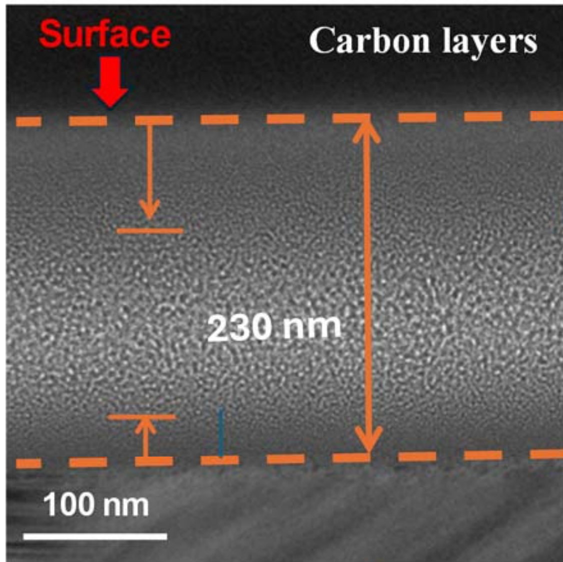
Surface
Carbon layers
230 nm
100 nm

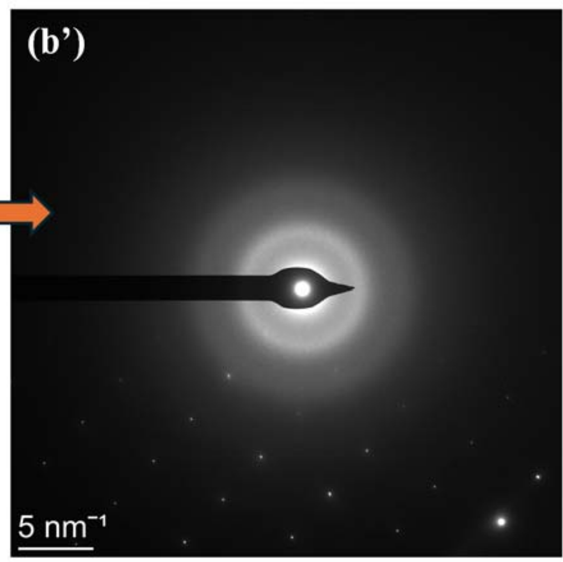
(b')
5 nm⁻¹

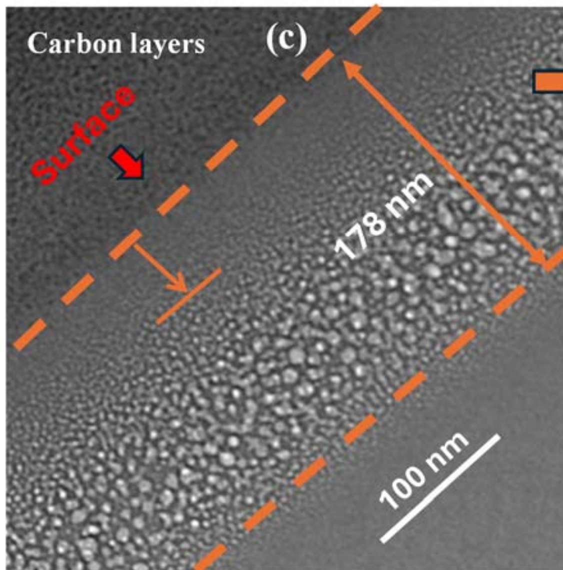
Carbon layers
(c)
Surface
178 nm
100 nm

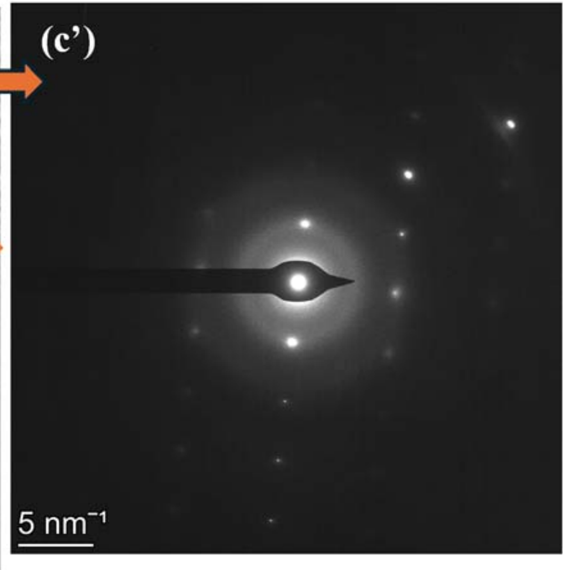
(c')
5 nm⁻¹

Fig. 5: *Cross-sectional BF TEM micrographs of (a) Se-implanted polycrystalline SiC at room temperature (RT) in focused mode, and subsequently implanted with He ions at (b) RT (under focused mode) and (c) 500 °C (under focused mode). SAED patterns (a'), (b'), and (c') were obtained from the damaged layers, indicated by double arrows in (a), (b), and (c), respectively. SRIM simulated results are included for comparison.*

Fig. 6 shows the cross-sectional bright-field (BF) TEM micrographs of Se implanted and the RT co-implanted samples, after annealing at 1000 °C. The figures also show SAED patterns in the damaged regions of the samples. TEM micrograph of the 500 °C co-implanted SiC samples is shown in Fig. 6 (c). Comparing the SAED patterns from Fig. 6 (a') with Fig. 5 (a'), it is clear that annealing caused recrystallization of Se implanted SiC. This was accompanied by a decrease in the damaged layer thickness. Epitaxial growth of amorphous SiC from the amorphous-crystalline interface may explain this thickness decrease [21]. The thickness of the damaged layer also decreased in the co-implanted samples after annealing, as shown in Fig. 5 and 6. However, three layers with a total thickness of 230 nm in the RT co-implanted samples were observed (in addition to the platinum layer) after annealing at 1000 °C. In the first layer (bright layer, thickness 44 nm), SAED pattern revealed the presence of an amorphous structure, while EDS mapping results (not shown) confirmed the presence of platinum and gallium atoms in this layer. This indicates that the first layer consists of platinum that has been damaged by Ga ions during the lamella thinning process. In addition, EDS showed that the other two layers were SiC, and SAED patterns confirmed that the layers were recrystallized. However, the structure of these layers was different. In Fig. 6 (b), the first SiC layer, with a thickness of 70 nm, showed a less defective structure than the second SiC layer, with a thickness of 122 nm. This could be explained by the initial structure (shown in Fig. 5 (b)) where no He bubbles formed in the near surface region. Therefore, after annealing, the region near the surface would recrystallize faster than areas with He bubbles which creates stresses in their region as discussed in Fig. 3. In cross-sectional BF TEM micrographs, light elements transmit a large number of electrons and appear brighter, confirming that the second SiC layer may contain a higher concentration of He. However, variations in orientation and defects may also result in different numbers of transmitted electrons, causing variation in contrast in the BF TEM micrograph. Moreover, by comparing Fig. 6 (b) with Fig. 5 (b), it appears that He bubbles

within the implanted region are still present even after annealing at 1000 ℃, a phenomenon also observed in a previous study [25]. The presence of He bubbles in the second layer of the co-implanted samples annealed at 1000 °C is further confirmed in Fig. 7, which shows the cross-sectional bright-field (BF) TEM micrographs in under focused mode. Additionally, Se atoms might also inhibit SiC recrystallization in the second layer aside from He bubbles. As predicted by SRIM, the maximum distribution of Se in SiC before annealing is within the second SiC layer as shown in Fig. 6 (b). The distribution of Se in the Se implanted and co-implanted samples was not observed from TEM results, therefore, RBS was conducted to investigate Se migration which is discussed in section 3.3.

From Fig. 6 (b), it is clear that annealing the 500 °C co-implanted samples at 1000 °C resulted in the formation of long strings of small bubbles accompanied by the formation of a thin low-defect layer (i.e., 34 nm) near the surface. However, the thickness of the low-defect layer in the RT co-implanted samples (i.e., 70 nm) annealed at 1000 ℃ is two times thicker than the one observed in the 500 °C co-implanted samples annealed under the same conditions (see Fig. 6 (b and c)). This could be attributed to the initial He distribution, where He bubbles appeared closer to the surface in the 500 ℃ co-implanted samples (from 52 to 178 nm below the surface) compared to the RT co-implanted samples (from 75 to 200 nm below the surface). Therefore, this suggests that the initial He distribution can have a large impact on the thickness of the recrystallized layer near the SiC surface.

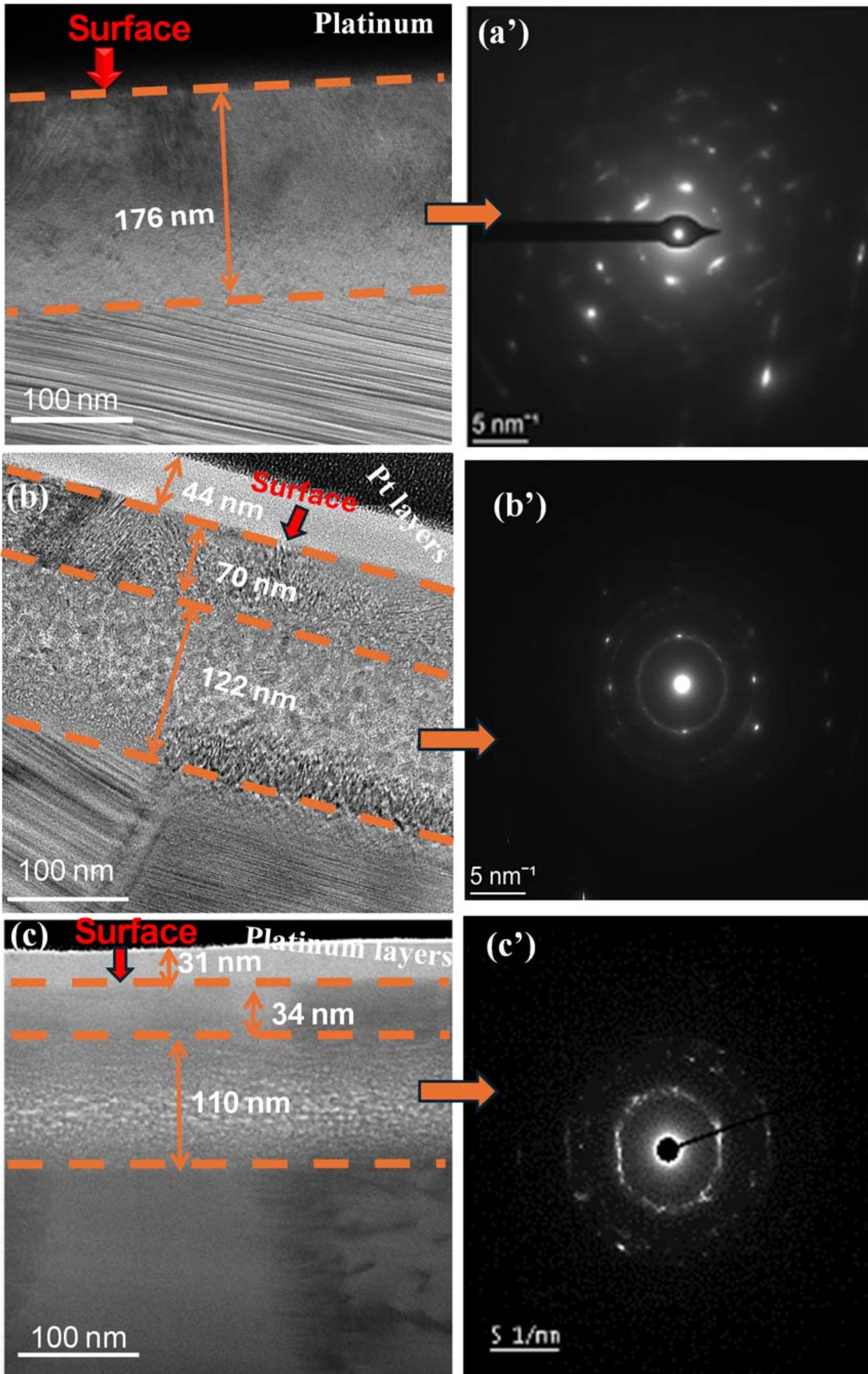
Surface
Platinum
176 nm
100 nm
(a')
5 nm⁻¹
(b)
44 nm
Surface
Pt layers
70 nm
122 nm
100 nm
(b')
5 nm⁻¹
(c)
Surface
Platinum layers
31 nm
34 nm
110 nm
100 nm
(c')
5 1/nm

Fig. 6: *Cross-sectional bright-field (BF) TEM micrographs of SiC: (a) implanted with Se at room temperature (RT) and annealed at 1000 °C (focused mode), (b) co-implanted with Se and He at RT and annealed at 1000 °C (focused mode), and (c) implanted with Se at RT and co-implanted with He at 500 °C, then annealed at 1000 °C (focused mode). SAED patterns (a'), (b'), and (c') were taken from the damaged regions.*

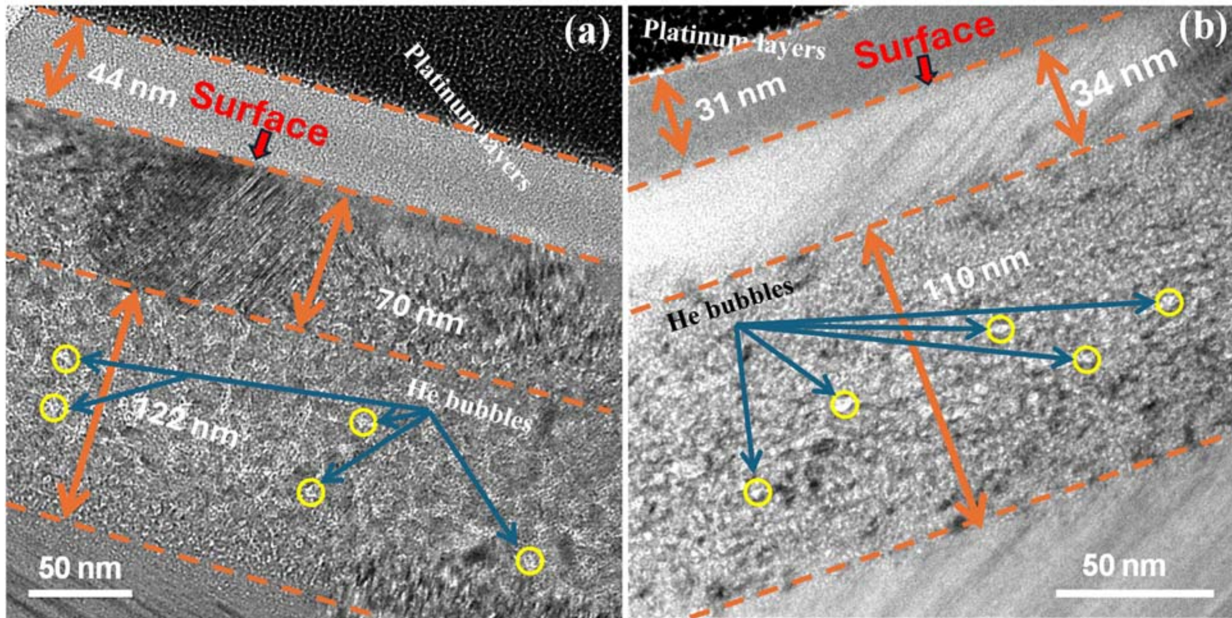

Fig. 7: *Cross-sectional BF-TEM micrographs (under focused mode) of (a) SiC co-implanted with Se and He at room temperature (RT) and annealed at 1000 °C, and (b) SiC implanted with Se at RT followed by He co-implantation at 500 °C and annealing at 1000 °C.*

3.3. RBS results:

Fig. 8 shows the effect of He implantation and annealing on the depth profile of Se in the SiC samples. Subsequent He implantation at RT and 500 °C did not result in any detectable change in the implanted Se profile, indicating no migration of implanted Se after co-implantation, as can be seen in Fig. 8 (a). Moreover, no Se migration was observed in the Se implanted samples annealed at 1000°C - see Fig. 8 (b). This agrees with the previous results [33-35], where Se non-diffusivity in SiC was observed after annealing from 1000 to 1200 °C. However, annealing at higher temperatures (≥1300 °C) showed detectable Se migration toward the SiC surface [33-35].

From Fig. 8 (c and d), annealing the co-implanted samples at 1000 °C caused the peak maximum of the depth profile to shift toward the SiC bulk accompanied by broadening in the FWHM – see Fig. 9 (a). This indicates that Se migrated toward the SiC bulk after annealing at 1000 °C. By comparing Se depth profiles with TEM micrographs in Fig. 7 (a and b), it is evident that Se migrated to regions containing He bubbles. Since no Se migration in Se implanted SiC samples was observed after annealing at 1000 °C (see Fig. 8 (b)), thus, this study suggests that He assisted Se migration in SiC. Additionally, since He bubbles create tensile stress (as discussed in Fig. 3), the migration of Se toward the He region is probably caused by the stress field [54]. Furthermore, since He creates high defective regions in SiC [28, 55], the migration of Se toward the He region may also be related to the strong binding energy between vacancies and impurities in SiC.

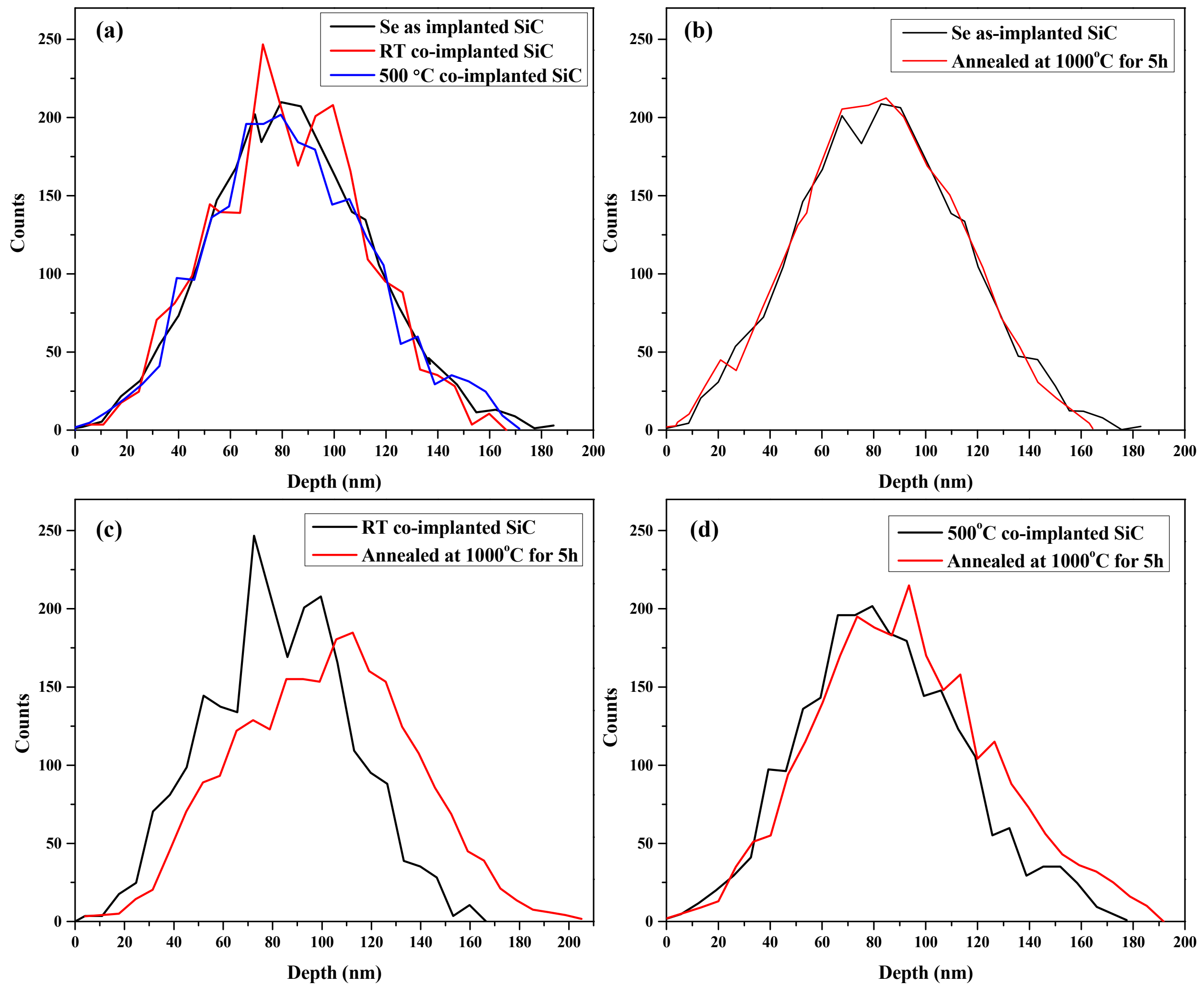

Fig. 8: *(a) Se depth profiles of individual and co-implanted SiC samples before annealing; (b) Se depth profiles of the individually implanted SiC before and after annealing at 1000°C; (c) Se depth*

profiles of the SiC co-implanted at room temperature (RT) before and after annealing at 1000°C; and (d) Se depth profiles of SiC co-implanted at 500°C before and after annealing at 1000°C.

Fig. 9 (a) shows the changes in the FWHM of the Se depth profile after co-implantation and annealing. No change in the FWHM of the Se depth profile after co-implantation at RT and 500 °C, indicating that He alone did not cause any migration of Se atoms in SiC. Moreover, annealing Se implanted samples at 1000 °C caused no significant change in the FWHM due to the non-diffusivity of Se atoms at this temperature [33-35]. However, the FWHMs of Se depth profiles in the co-implanted samples increased significantly after annealing at 1000 °C due to the migration of Se toward the bulk of SiC as shown in Fig. 8 (c and d). In RT co-implanted samples, the FWHM is wider than in 500 °C co-implanted samples, indicating more Se atoms migrate into the bulk. This could be due to the thicker highly defective region (i.e., second SiC layer) in the RT co-implanted samples than in the 500°C co-implanted samples observed by TEM (see Fig. 6) which can facilitate Se migration toward the bulk. In addition, no loss of Se atoms was observed in all samples annealed at 1000 °C - see Fig. 9 (b).

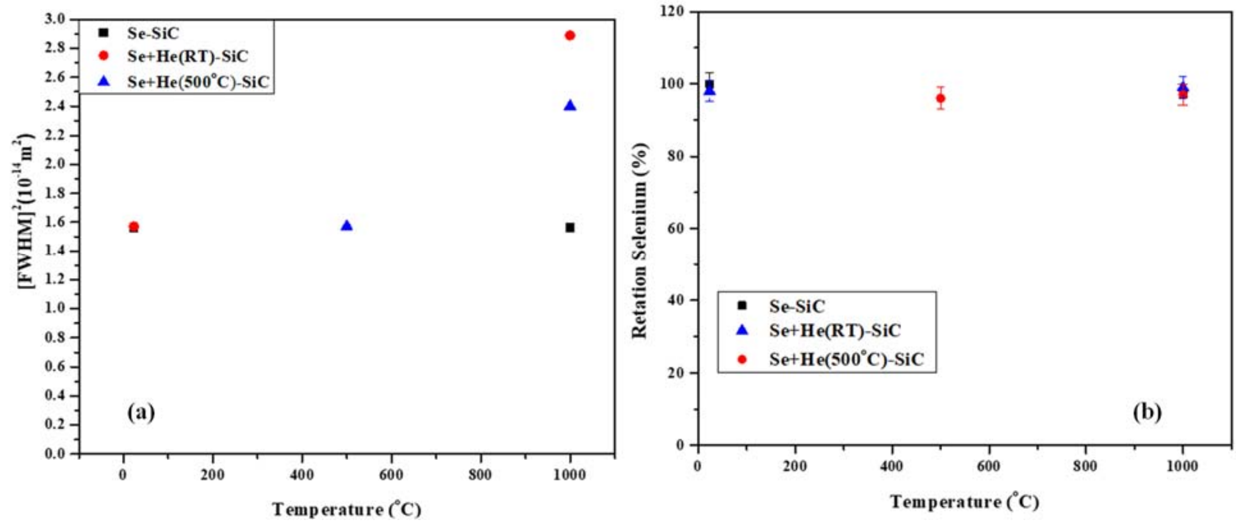

Fig. 9: *(a) FWHMs of Se depth profiles in SiC after co-implantation and annealing. (b) retention ratio of Se before and after annealing at 1000 ^{o}C.*

When comparing the current results with our previous studies, where Sr ions were co-implanted with He in SiC at different temperatures (both implantation of Sr and He at room temperature [RT] [26], and Sr at 600 °C followed by He at 350 °C [25]), and annealed at 1000 °C, similar recrystallization mechanisms were observed in the SiC co-implanted samples. Carbon D and G peaks were observed in the implanted region of SiC co-implanted with Sr and He at RT and annealed at 1000 °C [26]. This result aligns with our findings (see section 3.1, Fig. 2), where annealing at 1000 °C led to the appearance of D and G carbon peaks in the RT co-implanted samples. Furthermore, Mokgadi *et al.* [26] found that He assisted the migration of Sr in RT co-implanted SiC samples annealed at 1000 °C for 5 hours, whereas limited Sr migration was observed in Sr-implanted SiC samples annealed under the same conditions. This observation is also consistent with our results (see section 3.3, Fig. 8), where He facilitated the migration of Se in the co-implanted SiC after annealing at 1000 °C for 5 hours.

On the other hand, SiC implanted with Sr at 600 °C, then co-implanted with He at 350 °C, exhibited fewer defects than the samples co-implanted at RT [25, 26]. A similar observation was made in Fig. 2, where RT co-implanted samples showed more defects than those implanted at 500 °C, which exhibited some recrystallization. This was attributed to the implantation temperature, which allowed the defects to recover after co-implantation at 500 °C. Additionally, Mokgadi *et al.* [26] found that annealing co-implanted samples (i.e., Sr at 600 °C followed by He at 350 °C) at 1000 °C produced a less defective layer near the surface (approximately 75 nm in thickness), accompanied by the formation of large He bubbles, while Sr migrated toward the SiC bulk. The migration of Sr toward the SiC bulk in these co-implanted samples (Sr at 600 °C followed by He at 350 °C) was attributed to the growth of He bubbles after annealing, which facilitated Sr diffusion [25]. Similarly, He bubbles assisted in Se migration in SiC, as observed in our TEM and RBS results (see Figs. 6-8).

Moreover, a decrease in Sr and He concentrations was observed after annealing the RT co-implanted samples (Sr+He-SiC) at 1000 °C [26], while no similar loss was observed in Se concentration in RT co-implanted SiC samples annealed under the same conditions – see Fig. 8 (b). The difference in migration behavior between Se and Sr in RT co-implanted samples annealed at 1000 °C could be attributed to the fact that Sr is known to be more mobile in SiC than Se [10, 20, 26], where no diffusion of Se was observed in SiC after annealing at 1000 °C [33-35]. This

may be explained by the differences in the atomic sizes of implanted species (where Se has a smaller atomic size than Sr), the number of defects introduced into SiC by different implanted ions, and recrystallization behaviours.

4. Conclusion

Polycrystalline SiC samples were co-implanted with Se (at RT) and He (separately at RT and 500 °C) ions to investigate the microstructural changes and migration behavior of Se before and after annealing. Raman spectroscopy showed that implantation of Se ions alone created an amorphous layer in the SiC substrate, while subsequent implantation of He at RT resulted in the formation of free carbon in an initially amorphized SiC. This was due to the lower migration energy of carbon atoms (compared to Si atoms) which migrate more easily and accumulate in clusters after He implantation at RT. However, co-implantation at 500 °C caused recrystallization of initially amorphous SiC. Moreover, annealing at 1000 °C significantly enhanced recrystallization in both as-implanted and 500 °C co-implanted samples, while RT co-implanted samples experienced limited recrystallization due to graphitization. This was accompanied by the formation of long strings of He bubbles seen in TEM micrographs of co-implanted samples annealed at 1000 ℃. Moreover, He bubbles in SiC caused tensile stresses in the implanted region, which affected the average residual stress measured by Raman spectroscopy. These results suggest that the implantation temperature of He in SiC plays a significant role in SiC structure before and after annealing.

TEM analysis and SAED patterns supported Raman results by showing that Se implantation created an amorphous layer with 189 nm thickness. Moreover, co-implantation with He at RT increased the amorphized layer thickness to 230 nm with the formation of nano-bubbles within the implanted region, while He implantation at 500 ℃ reduced the amorphous layer thickness to 178 nm and caused recrystallization accompanied by the formation of long strings of He bubbles. Annealing at 1000 °C also reduced the amorphous thickness of the Se implanted samples (from 189 to 170 nm) with recrystallization observed within the shrank layer. On the other hand, annealing the co-implanted samples at 1000 °C caused the formation of two layers within the implanted layer. The near surface layer showed low defective structures with thicknesses of 34 and 70 nm for the RT and 500 ℃ co-implanted samples, respectively, annealed at 1000 ℃. The

difference in thickness of the low defective layer between co-implanted samples was attributed to the initial He distribution, where the depth of He atoms was shallower in the 500 ℃ co-implanted samples than in the RT co-implanted samples. The shallow He bubbles inhibit the recrystallization of the near surface region in the 500 ℃ co-implanted samples. The second thick layer showed a high defective structure accompanied by the formation of long strings of He bubbles. Thus, it confirms the fact that He atoms accumulate in defect regions (i.e., vacancies/interstitials).

Rutherford backscattering spectrometry (RBS) revealed significant migration of Se atoms towards the bulk of the SiC in co-implanted samples after annealing at 1000 °C, contrasting with the negligible migration observed in Se-only implanted samples annealed under the same conditions. This suggests that He assisted Se migration in SiC. Moreover, no loss of Se atoms was observed.

Declaration of Competing Interest

The authors declare that they have no known competing financial interests or personal relationships that could have appeared to influence the work reported in this paper.

Acknowledgements

This study was financially supported by the National Research Foundation (NRF) of South Africa (grant numbers: 2204072593, 30308881411 and 23040388976) and the University of Zululand (grant number: D066) which is gratefully acknowledged. We would like to thank Dr Jacques H O'Connell from the HRTEM center at Nelson Mandela Metropolitan University, and Dr A. Sohatsky from the Joint Institute for Nuclear Research for their assistance with TEM specimen preparation and viewing of images.

References

[1] J.L. Holechek, H.M. Geli, M.N. Sawalhah, R. Valdez, A global assessment: can renewable energy replace fossil fuels by 2050?, Sustainability. 14 (2022) 4792.

[2] R.E. Sims, H.H. Rogner, K. Gregory, Carbon emission and mitigation cost comparisons between fossil fuel, nuclear and renewable energy resources for electricity generation, Energy policy, 31 (2003) 1315-1326.

[3] D.A. Petti, P.A. Demkowicz, J.T. Maki, R.R. Hobbins, TRISO-Coated particle fuel performance, Compr. Nucl. Mater. 3 (2012) 151-213.

[4] J.B. Malherbe, E. Friedland, N.G. van der Berg, Ion beam analysis of materials in the PBMR reactor, Nucl. Instrum. Methods Phys. Res. B. 266 (2008) 1373-1377.

[5] J.B. Malherbe, Topical Review: diffusion of fission products and radiation damage in SiC, J. Phys. D Appl. Phys. 46 (2013) 473001.

[6] K. Verfondern, H. Nabielek, J.M. Kendall, Coated particle fuel for high Temperature gas cooled reactors, Nucl. Eng. Des. 39 (2007) 603-616.

[7] L.L. Snead, T. Nozawa, Y. Katoh, T.-S. Byun, S. Kondo, D.A. Petti, Handbook of SiC properties for fuel performance modeling, J. Nucl. Mater. 371 (2007) 329–377.

[8] T. Yano, T. Iseki, High-resolution electron microscopy of neutron-irradiation-induced dislocations in SiC Philos. Mag. A. 62 (1990) 421.

[9] TECDOC- 978, Fuel Performance and Fission Product Behaviour in Gas-Cooled Reactors, Tech. rep, IAEA, Vienna (1997). Available from:https://www.iaea.org/publications/5633/fuel-performance-and-fission-product-behaviour-in-gascooled-reactors.

[10] E. Friedland, N.G. van der Berg, J.B. Malherbe, E. Wendler, W. Wesch, Influence of radiation damage on strontium and iodine diffusion in silicon carbide, J. Nucl. Mater. 425 (2012) 205-210.

[11] B.P. Collin, Diffusivities of Ag, Cs, Sr, and Kr in TRISO Fuel Particles and Graphite. No. INL/EXT-16-39548, Idaho National Lab.(INL), Idaho Falls, ID (United States) (2016).

[12] T.T. Hlatshwayo, N. Mtshonisi, E.G. Njoroge, M. Mlambo, M. Msimanga, V.A. Skuratov, J.H. O'Connell, J.B. Malherbe, S.V. Motloung, Effects of Ag and Sr dual ions implanted into SiC, Nucl. Instrum. Methods Phys. Res. B. 472 (2020) 7-13.

[13] S. Dwaraknath, G.S. Was, The diffusion of cesium, strontium, and europium in silicon carbide, J. Nucl. Mater. 476 (2016) 155-167.

[14] T.T. Hlatshwayo, J.B. Malherbe, N.G. Van Der Berg, A.J. Botha, P. Chakraborty, Effect of thermal annealing and neutron irradiation in 6H-SiC implanted with silver at 350 °C and 600 °C, Nucl. Instrum. Methods Phys. Res. B. 273 (2012) 61–64.

[15] H. Nabielek, P.E. Brown, P. Offermann, Silver release from coated particle fuel, Nucl. Technol. 35 (1977) 483–493.

[16] J.H. Neethling, J.H. O'Connell, E.J. Olivier, Palladium assisted silver transport in polycrystalline SiC, Nuclear Engineering and Design. 251 (2012) 230-234.

[17] J. H. O'Connell, J. H. Neethling, Palladium and ruthenium supported silver migration in 3C–silicon carbide, J. Nucl. Mater. 456 (2015) 436-441.

[18] N. Chen, Q. Peng, Z. Jiao, I. Van Rooyen, W.F. Skerjanc, F. Gao, Analytical bond-order potential for silver, palladium, ruthenium and iodine bulk diffusion in silicon carbide, Journal of Physics: Condensed Matter. 32 (2019) 085702.

[19] H.A.A. Abdelbagi, V.A. Skuratov, S.V. Motloung, E.G. Njoroge, M. Mlambo, J.B. Malherbe, J.H. O'Connell, T.T. Hlatshwayo, Effect of swift heavy ions irradiation in the migration of silver implanted into polycrystalline SiC, Nucl. Instrum. Methods Phys. Res. B. 461(2019) 201-209.

[20] H.A.A. Abdelbagi, V.A. Skuratov, S.V. Motloung, E.G. Njoroge, M. Mlambo, T.T. Hlatshwayo, J.B. Malherbe, Effect of swift heavy ions irradiation on the migration behavior of strontium implanted into polycrystalline SiC, Nucl. Instrum. Methods Phys. Res. B. 451 (2019) 113-121.

[21] T.S. Mabelane, M. Sall, Z.A.Y. Abdalla, V.A. Skuratov, T.T. Hlatshwayo, Effect of 710 MeV Bi^{+51} swift heavy ions irradiation on Se pre-implanted polycrystalline SiC, Vacuum. 224 (2024) 113189.

[22] M.R. Gilbert, J.C. Sublet, Neutron-induced transmutation effects in W and W-alloys in a fusion environment, Nucl. Fusion. 51 (2011) 043005.

[23] T.T. Hlatshwayo, C.E. Maep, M. Msimang, M. Mlamb, E.G. Njoroge, V. A. Skuratov, S.V. Motloung, J.B. Malherbe, Helium assisted migration of silver implanted into SiC, Vacuum. 183 (2021) 109865.

[24] S.Z. Mtsi, A. Sohatsky, Z.A.Y. Abdalla, E.G. Njoroge, V.A. Skuratov, S.V. Motloung, J.B. Malherbe, T.T. Hlatshwayo, Effects of helium (He) bubbles and annealing on the structural evolution and migration behavior of silver (Ag) implanted into polycrystalline SiC at 350 °C, Vacuum. 218 (2023) 112621.

[25] T.F. Mokgadi, Z.A.Y. Abdalla, M. Madhuku, E.G. Njoroge, M. Mlambo, P. Mdluli, A. Sohatsky, V.A. Skuratov, J.B. Malherbe, T. T. Hlatshwayo, The influence of helium-induced defects on the migration of strontium implanted into SiC above critical amorphization temperature, Frontiers in Materials. 10 (2023) 1192989.

[26] T. Mokgadi, Z. Abdalla, H. Abdelbagi, M. Msimanga, C. Maepa, V. Skuratov, T. Hlatshwayo, Helium and strontium co-implantation into SiC at room temperature and isochronal annealing: structural evolution of SiC and migration behaviour of strontium. Materials Chemistry and Physics. 294 (2023) 126998.

[27] M. Liu, H. Gong, W. Liu, R. Liu, and J. Cao, Effects of He on the recrystallization and Mg diffusion in Mg ion implanted CVD-SiC, Journal of Nuclear Materials. 545 (2021) 152747.

[28] B.S. Li, H.S. Sen, N. Daghbouj, A.T. AlMotasem, J. Lorinčík, M. Karlik, F.F. Ge, L. Zhang, Z. Sofer, I. Elantyev, M. Callisti, Thermal behavior of iron in 6H-SiC: influence of He-induced defects. Scr. Mater. 218 (2022) 114805.

[29] M.F. Beaufort, M. Vallet, J. Nicola, E. Oliviero, J.F. Barbot, In-situ evolution of helium bubbles in SiC under irradiation, J. Appl. Phys. 118 (2015) 205904.

[30] L. Yang, X.T. Zu, H.Y. Xiao, F. Gao, H.L. Heinisch, R.J. Kurtz, Defect production and formation of helium–vacancy clusters due to cascades in α-iron, Phys. B Condens. Matter. 391 (2007) 179-185.

[31] P. Bienvenu, P. Cassette, G. Andreoletti, M.M. Bé, J. Comte, M.C. Lépy, A new determination of ^{79}Se half-life, App. Rad. Iso. 65 (2007) 355.

[32] Argonne National Laboratory. Radiological and Chemical Fact Sheets to Support Health Risk Analyses for Contaminated areas, Human Health Fact Sheet, August 2005.

[33] Z.A.Y. Abdalla, M.Y.A. Ismail, E.G. Njoroge, T.T. Hlatshwayo, E. Wendler, J.B. Malherbe, Migration behaviour of selenium implanted into polycrystalline 3C–SiC, Vacuum. 175 (2020) 109235.

[34] Z.A.Y. Abdalla, M.Y.A. Ismail, E.G. Njoroge, E. Wendler, J.B. Malherbe, T.T. Hlatshwayo, Effect of heat treatment on the migration behaviour of selenium implanted into polycrystalline SiC, Nuclear Inst. and Methods Phys Res B. 487 (2021) 30.

[35] Z.A.Y. Abdalla, E.G. Njoroge, M. Mlambo, S.V. Motloung, J.B. Malherbe, T.T. Hlatshwayo, Isothermal annealing of selenium (Se)-implanted silicon carbide: structural evolution and migration behavior of implanted Se, Mat. Chem. Phys. 276 (2022) 12533.

[36] E. Friedland, J.B. Malherbe, N.G. van der Berg, T.T. Hlatshwayo, A.J. Botha, E. Wendler, W. Wesch, Study of Silver diffusion in silicon carbide, J. Nucl. Mater. 389 (2009) 326-331.

[37] J.F. Ziegler, M.D. Ziegler, J.P. Biersack, SRIM–The stopping and range of ions in matter (2010), NuclNuclear Inst. and Methods Phys Res B. 268 (2010) 1818.

[38] W.J. Weber, N. Yu, L.M. Wang, Structure and properties of ion-beam-modified (6H) silicon carbide, J. Nucl. Mater. 53 (1998) 253.

[39] W.J. Weber, L.M. Wang, N. Yu, The irradiation-induced crystalline-to-amorphous phase transition in α-SiC.Nucl. Instrum. Methods Phys. Res B. 116 (1996) 322-326.

[40] K. J. Stevenson, Review of originpro 8.5, Journal of the American Chemical Society. 133 (2011) 5621.

[41] S. Lin, Z. Chen, L. Li, C. Yang, Effect of impurities on the Raman scattering of 6H-SiC crystals, Materials Research. 15 (6) (2012) 833–836.

[42] D.N. Talwar, Probing optical, phonon, thermal and defect properties of 3C–SiC/Si (001), Diamond and Related Materials. 52 (2015) 1–10.

[43] W. Windl, K. Karch, P. Pavone, O. Schütt, D. Strauch, W.H. Weber, K.C. Hass, L. Rimai, Second-order Raman spectra of SiC: Experimental and theoretical results from ab initio phonon calculations, Phys. Rev. B. Condens. Matter. 49 (1994) 8764–8767.

[44] B. Li, C. Zhang, H. Liu, L. Xu, X. Wang, Z. Yang, F. Ge, W. Gao, T. Shen, Microstructural and elemental evolution of polycrystalline α-SiC irradiated with ultra-high-fluence helium ions before and after annealing, Fusion Engineering and Design. 154 (2020) 111511.

[45] W.T. Han, H.P. Liu, B.S. Li, Transmission electron microscopy and high-resolution electron microscopy studies of structural defects induced in Si single crystals implanted by helium ions at 600°C, Appl. Surf. Sci. 455 (2018) 433–437.

[46] Z. Xu, Z. He, Y. Song, X. Fu, M. Rommel, X. Luo, A. Hartmaier, J. Zhang and F. Fang, Application of Raman spectroscopy characterization in micro/nanomachining, Micromachines 9 (2018) 361.

[47] A.J. Leide, R.I. Todd, D.E. Armstrong, Measurement of swelling-induced residual stress in ion implanted SiC, and its effect on micromechanical properties, Acta Materialia. 196 (2020) 78-87.

[48] E. Wendler, A. Heft, W. Wesch, Ion-beam induced damage and annealing behaviour in SiC, Nucl. Instrum. Methods Phys. Res. B. 141 (1998) 105–117.

[49] K. Konishi, R. Fujita, Y. Mori, A. Shima, Inducing defects in 3.3 kV SiC MOSFETs by annealing after ion implantation and evaluating their effect on bipolar degradation of the MOSFETs, Semiconductor Science and Technology. 33 (2018) 125014.

[50] H.A.A. Abdelbagi,T.A.O. Jafer, V.A. Skuratov, E.G. Njoroge, M. Mlambo, T.T. Hlatshwayo, J.B. Malherbe, Effects of swift heavy ion irradiation and annealing on the microstructure and recrystallizationof SiC pre-implanted with Sr ions, Frontiers in Nuclear Engineering. 1 (2022) 1034114.

[51] K.M.Tynyshbayeva, K.K. Kadyrzhanov, A.L. Kozlovskiy, Y.I. Kuldeyev, V. Uglov, M.V. Zdorovets, Study of helium swelling and embrittlement mechanisms in SiC ceramics, Crystals. 12 (2022) 239.

[52] J. Aihara, T. Hojo, S. Furuno, M. Ishihara, K. Sawa, H. Yamamoto, K. Hojou, Recrystallization behavior in SiC amorphized with He or Ne irradiation, Nucl. Instrum. Methods Phys. Res. B. 241 (2005) 559-562.

[53] H.A.A. Abdelbagi, V.A. Skuratov, S.A. Adeojo, T.M. Mohlala, T.T. Hlatshwayo, J.B. Malherbe, Effect of SHI irradiation and high temperature annealing on the microstructure of SiC implanted with Ag, Nucl. Instrum. Methods Phys. Res. B. 511 (2022) 18-29.

[54] S. Nsengiyumva, A.T. Raji, J.P. Riviere, D.T. Britton, M. Harting, Stress enhanced diffusion of krypton ions in polycrystalline titanium, J. Appl. Phys. 116 (2014) 023513.

[55] H.S. Sen, N. Daghbouj, B. Li, A.T. AlMotasem, F. Ge, L. Zhang, M. Callisti, T. Polcar, Interaction of Stacking Faults with Point/Extended Defects in Fe-He Irradiated 6H-SiC, Acta Mater. 256 (2023) 119129.